MASTER THESIS

International double-degree Master's program

NANOTECHNOLOGIES AND QUANTUM DEVICES

Semiconductor Saturable Absorber Mirrors in the mid-IR

Candidate:

Eduardo Cosentino

Academic supervisors:

Carlo Ricciardi, Maria Luisa Della Rocca

Internship supervisors:

Raffaele Colombelli, Mathieu Jeannin, Jean Michel Manceau

Hosting institution:

Centre de Nanosciences
et de Nanotechnologies – C2N

A joint research unit

July 1, 2022 – Academic year 2021/2022

Acknowledgment

I would like to express my uttermost gratitude to my supervisors Raffaele Colombelli, Mathieu Jeannin and Jean Michel Manceau for their support throughout my internship at C2N. I extend my gratefulness to the whole ODIN group, whose members individually contributed to my growth inside the team and particularly to the intern students Luca and Abdelkrim. A special mention goes to my office mate Stefano Pirotta for having taught me the value of science through his citations and to Leonardo DiCaprio, who tirelessly watches over us.

I also thank all my NanoQuad fellows, who shared with me so many adventures in Paris and contributed to make this Erasmus an amazing experience. I sincerely wish you all the best.

Finally, I say a huge *grazie* to all my family in Italy who was always with me despite the distance and to my longtime friends who came to visit me in Paris, and to those who did not. But above all I want to thank my girlfriend Sara who helped me to overcome all the asperities of this journey and watched proudly to my achievements.

Presentation of the research framework

The present document summarizes part of the work that I have been carrying during the five-month internship (1 March 2022 – 31 July 2022) at the Centre de Nanosciences et de Nanotechnologies – C2N. The laboratory is a joint research unit between the CNRS and Université Paris-Saclay. It was founded on the 1st June 2016 by merging two former laboratories, the *Laboratoire de Photonique et de Nanostructures* (LPN) and the *Institut d'Electronique Fondamentale* (IEF). Its facility covers 18,000 m^2 and is able to boast 2,800 m^2 of clean room, where more than 400 people work, be they researchers, engineers, technicians and administrative staff. Its strong instrumentation activity makes C2N a world-class player in the development of new instruments for nanotechnology. It aims to establish a flagship laboratory for research in nanoscience and nanotechnology in the Ile-de-France region.

The center develops research in multiple scientific fields, covering all the range from fundamental to applied science. The laboratory is organized around four scientific departments: photonics, materials, nanoelectronics and microsystems and nanobiofluidics. My internship took place within the Photonics Department, in the Optoelectronic Devices and INnovation (ODIN) group. In particular the activity was carried in the MIR-THz Intersubband Devices team, under the close supervision of Mathieu Jeannin, Jean-Michel Manceau and the team leader Raffaele Colombelli. The goal of the MIR-THz research activity is to develop novel optoelectronic devices within the technologically under-developed part of the electromagnetic spectrum: from mid to far infrared, covering wavelengths from 3 μm to 300 μm. The way to operate is by exploring a solid state approach exploiting the electronic transitions between confined states in the conduction band of quantum wells (QWs), the so-called *intersubband transitions.* These transitions are keys to various devices such as quantum cascade lasers (QCL), polaritonic light emitting diode (LED) and quantum well infrared photodetectors (QWIP).

Contents

Chapter 1

Introduction

Infrared light (IR) is electromagnetic radiation with a wavelength ranging between 700 nm and 30 μm (frequency of 10 THz to 430 THz). The human eye is not sensitive to this frequency range since it lies above the nominal red extreme of the visible spectrum, however human body can perceive it as heat. The infrared band is further subdivided into smaller regions. In particular, the mid-infrared band (also denoted as mid-IR) shows frequencies ranging between 20 THz and 100 THz, with corresponding wavelength lying between 3 μm and 20 μm.

The mid-IR band is highly relevant for a broad set of applications. We can mention thermal imaging, that is used to remotely measure the temperature of an object and therefore to detect heat accumulation in devices or in industrial plants, as well as military applications. This technology relies on the fact that the black-body emission of an object around room temperature is peaked in the mid-IR range, returning a clear indication about its surface temperature. In addition, the mid-IR band is extensively used for pollutants detection through IR spectroscopy. This is made possible by the analysis of the rotational-vibrational modes of molecules induced by infrared excitation. The corresponding absorption lines are peculiar for each different molecule, denoting their so-called *molecular fingerprint*. Finally, the mid-IR band is of the utmost interest also in astronomy since infrared light in general is less sensitive to cosmic dust than the visible. The light coming from very early and distant cosmological objects arrives to the Earth strongly red-shifted. For this reason, the James Webb Space Telescope recently launched has been provided with a mid-IR detector allowing the detection of longer wavelength compared to previous space telescopes, such as Hubble, whose detection capabilities were limited to the near-IR.

1.1 Current challenges related to the mid-IR

Despite its high potential in terms of applications, widespread implementation of mid-IR spectroscopy still presents several challenges. On one hand, a practical solution for quantum detectors to be used in mid-IR spectroscopy is currently lacking. The most commonly employed technologies for this purpose are HgCdTe detectors – which represent the standard in industrial applications but are toxic because of the presence of mercury – and superconducting nanowire detectors which however require cryogenic cooling down to millikelvin temperature. On the other hand, the technology behind ultra-fast and compact sources of light in the mid-IR is not well established yet. With respect to this second challenge, the current state-of-the-art solution to achieve ultra-short pulses of light in the mid-IR is to use an optical parametric oscillator (OPO). This is however a cumbersome, energetically inefficient and expensive instrument. It relies on the conversion of a pump photon with frequency ω_p into two photons with frequencies ω_s and ω_i. To produce photons in the mid-IR range with an OPO, it is necessary to start with an external source of photons with higher energies – such as in the visible – and then to convert them to the desired wavelength, as reported in Ref. [1]. Part of the energy of the pump photon is inevitably lost in the conversion, making this an energetically inefficient way to produce photons in the mid-IR. Therefore, the goal would be to achieve sub-picosecond pulses with electrically pumped solid-state laser in the mid-IR, in a solution that is possibly compact, energetically efficient and ultra-fast.

Several applications could benefit from the introduction of such a laser source. For instance, mode-locked lasers are exploited in the generation of *frequency combs*, whose spectrum is constituted by a series of equidistant frequency lines emitted in trains of ultra-short pulses. This is widely used in spectroscopy to follow the dynamics of physical and chemical processes occurring at ultra-fast time scales, as well as for optical clocks. In addition, ultra-short pulses of light ensures the possibility to obtain high peak-power with mode-locked lasers.

1.2 Introduction to Saturable Absorber Mirrors

The achievement of ultra-short pulses of light in the visible and near-IR range has been made possible thanks to the introduction of semiconductor saturable absorber mirrors (SESAMs) [4]. They represent a revolutionary kind of mirrors showing non-linear reflectivity depending on the intensity of the incident light. The peculiar behavior of the SESAM reflectance is reproduced in Figure (1.1), showing low reflectivity at low intensity and high reflectivity at high intensity. More generally, a saturable absorber shows a non-linear absorption as the absorption coefficient α depends on the intensity I of the impinging radiation [2]:

$$\alpha = \frac{\alpha_0}{1 + I/I_{\text{sat}}}\ , \tag{1.1}$$

where α_0 is the absorption at low intensity and I_{sat} is the saturation intensity. The latter is defined as the value at which the absorption reaches half of its maximum excursion. In the particular case in which the absorption covers the widest possible range from 1 at low I to 0 at high I, then I_{sat} corresponds to a reflectance of 0.5.

However, the same concept holding for SESAMs in the visible and near-IR range cannot be transferred to the mid-IR range. Most SESAM devices demonstrated to date have operated in the near infrared wavelength range, typically between 0.8 to 2.4 μm [4, 9]. More recent works pushed the operation wavelength up to 4.6 μm using a single layer of HgCdTe [16], and to 5 μm using an InAs/GaSb type-II superlattice [8], making emerge the difficulties in increasing the wavelength any further. Nevertheless, SESAMs in the mid-IR would enable self-starting sources of ultra-fast pulses. Saturable absorbers in the visible and near-IR range rely either on bulk absorption, or interband absorption, involving

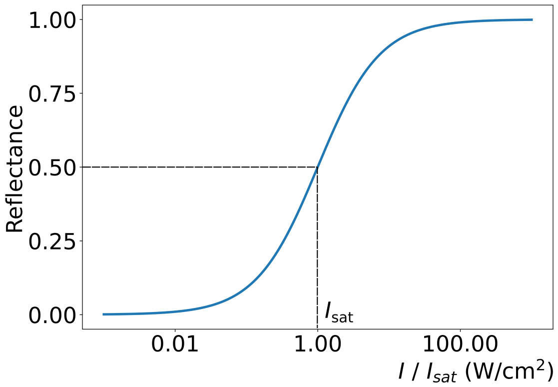

Figure 1.1: Non linear reflectivity of a SESAM, in the limit case of zero reflectance at low I and unitary reflectance at high I.

interband processes between the quantum confined levels of undoped heterostructures. Conversely, intersubband (ISB) SESAMs in the mid-IR range rely on transitions between quantum confined levels of doped heterostructures. In this case the absorption processes involve transitions within the same band, the conduction band for the present work. Whilst SESAMs in the visible and near-IR involving interband processes do exist, the same do not exist yet in the mid-IR powered by intersubband processes. Figure (1.2) shows the specific transitions required to obtain a SESAM structure depending on the photon energy.

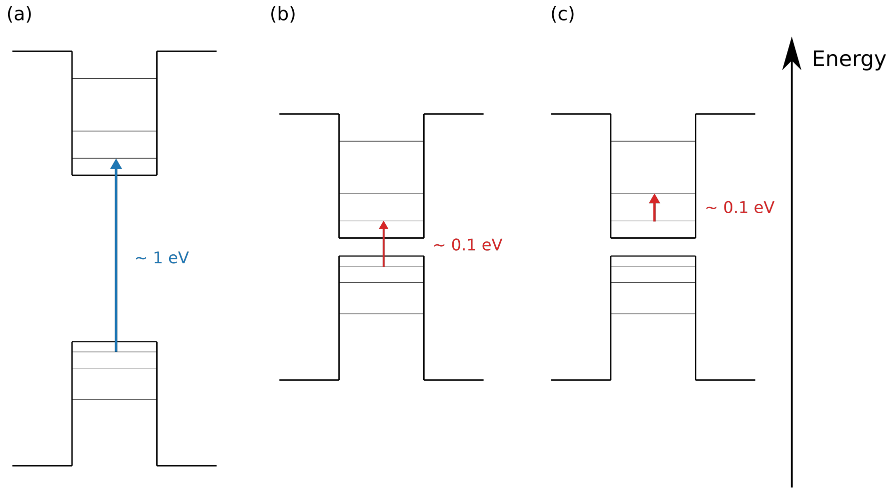

Figure 1.2: (a) Interband transition for visible and near-IR. (b) Interband transition for mid-IR, requiring a low band-gap semiconductor like HgCdTe. (c) Intersubband transition for mid-IR.

Chapter 2

Theory of intersubband microcavity polaritons

In this section, the main concepts about intersubband microcavity polaritons are exposed in order to set the ground to understand the strong light-matter coupling which occurs in the SESAMs, yielding absorption saturation. First, we will focus on the light-matter interaction occurring in a doped semiconductor quantum well and the corresponding intersubband transition. We then describe the properties of the metallic cavity in which the quantum well is embedded. Finally, the two concepts above will be merged to explain the onset of strong light-matter coupling, a regime in which the response is governed by coupled light-matter states called *polaritons*.

2.1 Light-matter interaction in a QW and intersubband (ISB) transitions

The Hamiltonian governing the interaction between a particle with charge q and mass m and an electromagnetic field with vector potential $\vec{A}$ and scalar potential Φ is:

$$\hat{H} = \frac{(\vec{p} - q\vec{A})^2}{2m} + V_c(\vec{r}) + q\Phi \ , \tag{2.1}$$

where $V_c(\vec{r})$ is the crystal potential to which the particle is subjected. The first step is to write the Hamiltonian above in the form $\hat{H} = \hat{H}_0 + \hat{H}_1(t)$, in which $\hat{H}_0$ can be treated within the envelope function approximation while on $\hat{H}_1(t)$ we will apply the Fermi golden rule. The latter is necessary to compute the transition rate between two quantum confined levels.

The usual way to proceed is to impose the Coulomb gauge to the light part of the interaction. This is done by posing $\vec{\nabla} \cdot \vec{A} = 0$ and $\Phi(\vec{r}) = 0$, meaning that now $\vec{p}$ and $\vec{A}$ commute. Within the Coulomb gauge, Equation (2.1) simplifies to:

$$\hat{H} = \frac{p^2}{2m} - \frac{q}{m}\vec{A}\cdot\vec{p} + \frac{q^2A^2}{2m} + V_c(\vec{r}) \approx \frac{p^2}{2m} + V_c(\vec{r}) - \frac{q}{m}\vec{A}\cdot\vec{p} = \hat{H}_0 + \hat{H}_1(\vec{r}, t) \ , \tag{2.2}$$

with $\hat{H}_0 = \frac{p^2}{2m} + V_c(\vec{r})$ and $\hat{H}_1(\vec{r}, t) = -\frac{q}{m}\vec{A}\cdot\vec{p}$. The quadratic term in A^2 is neglected by considering low intensity electromagnetic fields.

Let us consider now a plane wave polarized along $\vec{e}$ with wavevector $\vec{q}$:

$$\vec{E} = E_0 \cos(\vec{q}\cdot\vec{r} - \omega t)\,\vec{e} \ . \tag{2.3}$$

By integrating in time the expression above, one can retrieve the expression of the vector potential:

$$\vec{A} = \frac{E_0}{\omega} \sin(\vec{q} \cdot \vec{r} - \omega t)\, \vec{e}\,. \tag{2.4}$$

Within the *electric dipole approximation*, the wavelength of the light is considered much longer than the dimension of the system or, in the specific case, of the quantum well width. It follows that the photon wavevector can be neglected, thus the spatial dependence of $\vec{A}$ is lifted. This means that the photon gives a negligible contribution to the electron in terms of momentum when the two interact. Therefore, the time-dependent term of the interaction Hamiltonian reads:

$$\hat{H}_1(t) = \frac{qE_0}{m\omega}\, \vec{e} \cdot \vec{p} \sin(\omega t)\ , \tag{2.5}$$

which can be plugged in the Fermi golden rule to evaluate the optical transition rate between levels $|i\rangle$ and $|f\rangle$:

$$W_{i \to f} = \frac{2\pi}{\hbar} \left| \left\langle f \,\middle|\, \frac{qE_0}{m\omega}\, \vec{e} \cdot \vec{p} \,\middle|\, i \right\rangle \right|^2 \delta(E_f - E_i - \hbar\omega)\ . \tag{2.6}$$

Both $|i\rangle$ and $|f\rangle$ represent a confined state in a quantum well. The quantum numbers to describe them are (α, β) denoting the band, (n, m) denoting the subband and ($\vec{k}$, $\vec{k'}$) describing the electron momentum. Therefore, the transition rate in Equation (2.6) expresses the transition probability from state $|i\rangle = \left|\alpha, n, \vec{k}\right\rangle$ to state $|f\rangle = \left|\beta, m, \vec{k'}\right\rangle$. In other words:

$$W_{i \to f} \propto \left\langle \beta, m, \vec{k'} \,\middle|\, \vec{e} \cdot \vec{p} \,\middle|\, \alpha, n, \vec{k} \right\rangle\ . \tag{2.7}$$

Within the envelope function approximation, the electronic wavefunction in a heterostructure can be expressed as the product of a Bloch function in the Γ point and an envelope function supposed slowly varying compared to the material lattice constant. It follows:

$$\Psi(\vec{r}) = \left\langle \vec{r} \,\middle|\, \alpha, n, \vec{k} \right\rangle = u_{\alpha,\vec{0}}(\vec{r})\, \chi^{\alpha}_{n,\vec{k}}(\vec{r})\ . \tag{2.8}$$

As a consequence, the matrix element in Equation (2.6) can be divided in two parts:

$$\left\langle \beta, m, \vec{k'} \,\middle|\, \vec{e} \cdot \vec{p} \,\middle|\, \alpha, n, \vec{k} \right\rangle = \left\langle u_{\beta,\vec{0}} \,\middle|\, u_{\alpha,\vec{0}} \right\rangle \left\langle \chi^{\beta}_{m,\vec{k'}} \,\middle|\, \vec{e} \cdot \vec{p} \,\middle|\, \chi^{\alpha}_{n,\vec{k}} \right\rangle + \left\langle \chi^{\beta}_{m,\vec{k'}} \,\middle|\, \chi^{\alpha}_{n,\vec{k}} \right\rangle \left\langle u_{\beta,\vec{0}} \,\middle|\, \vec{e} \cdot \vec{p} \,\middle|\, u_{\alpha,\vec{0}} \right\rangle\ . \tag{2.9}$$

The first term accounts for the *intersubband transitions*, namely the transitions occurring within the same band, because the functions $u(\vec{r})$ build an orthonormal basis. The second term instead accounts for the *interband transitions*, which occur between valence and conduction band. The present work deals with the former, as defined in Figure (2.1) where the intersubband transition takes place between the first two quantum confined levels within the conduction band of a semiconductor quantum well, properly doped in order to host the majority of electrons in the first level. The term accounting for intersubband transitions then can be made explicit as follows, considering $\alpha = \beta$:

$$\left\langle \chi_{m,\vec{k'}} \,\middle|\, \vec{e} \cdot \vec{p} \,\middle|\, \chi_{n,\vec{k}} \right\rangle = \left\langle \chi_{m,\vec{k'}} \,\middle|\, \Big(e_x p_x + e_y p_y + e_z p_z \Big) \,\middle|\, \chi_{n,\vec{k}} \right\rangle\ , \tag{2.10}$$

where $\chi_{n,\vec{k}} = \frac{1}{\sqrt{S}}\, e^{i\vec{k}\cdot\vec{R}}\, \phi_n(z)$. Only the term $e_z p_z$ gives a non-zero contribution, yielding the well-known *polarization selection rule* for intersubband (ISB) transitions which states that a component of the light along the growth direction of the heterostructure is required to excite an intersubband transition. In other words, light coming perpendicularly to the plane of the QW is not able to induce an ISB transition. In addition, the *parity selection*

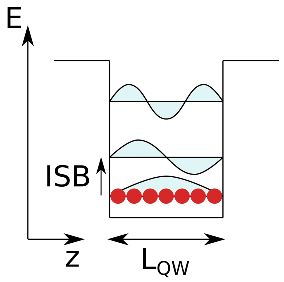

Figure 2.1: Intersubband transition within the conduction band of a doped semiconductor quantum well.

rule in the matrix element in Equation (2.10) implies that ϕ_n and ϕ_m must have different parity to allow ISB transition.

To express the weight of a specific ISB transition, the *oscillator strength* is commonly used:

$$f_{m,n} \overset{\text{def}}{=} \frac{2}{m^* E_{mn}} \Big| \langle \phi_m \,|\, p_z \,|\, \phi_n \rangle \Big|^2 = \frac{2m^* \omega_{m,n}}{\hbar} \Big| \langle \phi_m \,|\, z \,|\, \phi_n \rangle \Big|^2 \,. \tag{2.11}$$

The completeness of the eigenstate basis $\phi_n(z)$ implies that the sum of the oscillator strengths of all the possible ISB transitions is unitary:

$$\sum_m f_{m,n} = 1 \,. \tag{2.12}$$

The discussion above deals with the interaction of light with a single intersubband transition within the conduction band. However, whenever multiple transitions are taken into account, the electrons contained in the quantum well repel each other through Coulomb interaction. This reciprocal electronic perturbation belongs to the category of many-body effects, which is however beyond the purpose of this work. The main effect of this Coulomb interaction is to create a collective transition composed of the coherent sum of all single particle transitions, called *intersubband plasmon*. This gives rise to a *depolarization shift* of the many-body ISB transition frequency and an enhancement of the light-matter interaction [15, 6].

2.2 Dispersive and non-dispersive cavities

To enhance the light-matter interaction within the active region, the latter is embedded inside a cavity. The interaction scales as $\sqrt{N/V_{\text{eff}}}$ with V_{eff} the effective volume of the cavity mode and N the number of electrons (or dipoles) involved in the intersubband transition, which is directly related to the number of quantum well N_{QW} in the active region. In order to enhance the light matter interaction, a crucial step is therefore to design a cavity that produces an electric field in a very small volume within the cavity and at the same time fulfills the ISB selection rules derived in the previous section. In the mid-IR, this is well performed by metal-metal cavities, as depicted in Figure (2.2a). In these structures the electric field must satisfy the boundary conditions, thus the tangential component of $\vec{E}$ at the surface of the gold layers must vanish. In other words, the electric field is normal to the metal plane. In this way, the metal-metal cavity helps to rotate the direction of the electric field of the incoming light in order to enhance the optical response of the ISB transition embedded in the cavity.

On an array of cavities, the localized modes within each individual cavity can cross-talk with each others, yielding a delocalized electromagnetic pattern over the whole system, when the thickness L of the structures increases. The best way to represent this is by studying the dispersion diagram of the cavities array, that is how the eigenfrequency of the system depends on the parallel wavevector $k_{\parallel}$. In Figure (2.2b) are reported the dispersion diagrams of the structures for increasing thickness L. For larger values of the thickness, the cavities show dispersive behavior: the eigenfrequency depends on the normalized parallel wavevector, resulting in a cross-talk of the electromagnetic field confined in adjacent cavities. On the opposite, for extreme sub-wavelength thickness the dispersion relation is almost flat, yielding a *dispersionless* profile. In these non-dispersive cavities the electromagnetic field is localized within each structure.

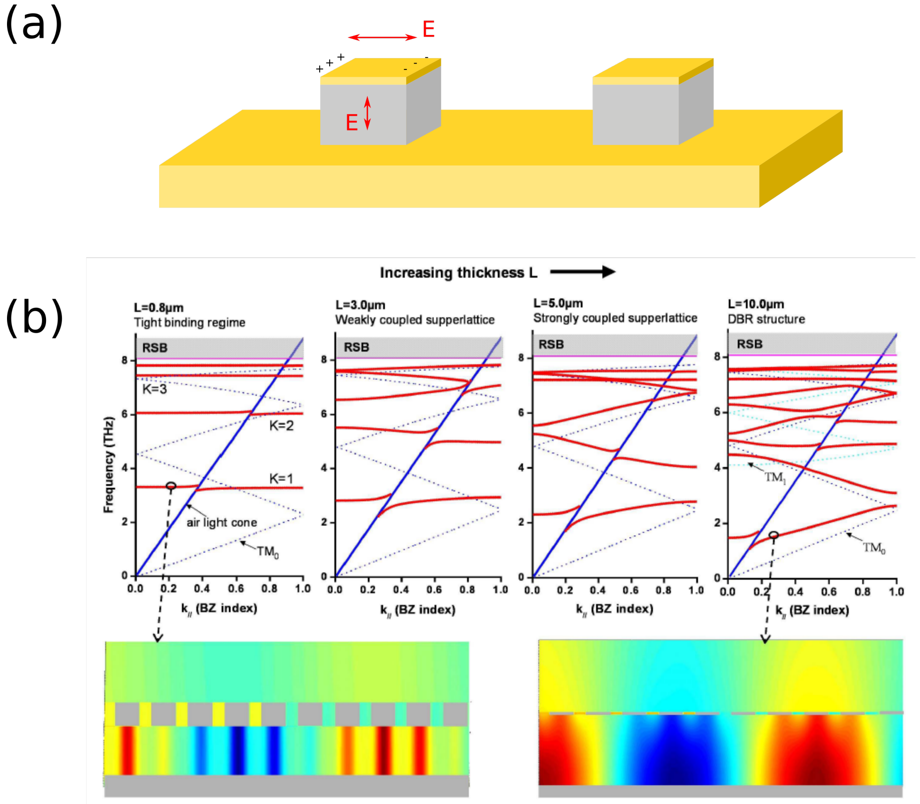

Figure 2.2: (a) Metal-metal cavities rotate the direction of the electric field of the incoming light. (b) Dispersion relations for cavities with increasing thickness and same sizes [12].

The case under study of this work involves non-dispersive, square 2D metallic cavities. The two-dimensional confinement produces an electric field distribution inside the cavities given by:

$$E_z(x,y) = E_{z0}\cos\left(\frac{\pi N}{s}x\right)\cos\left(\frac{\pi M}{s}y\right) \quad . \tag{2.13}$$

This results in a confinement of the electromagnetic field in all the three dimensions, yielding truly *dispersionless photonic modes* where the resonance frequencies are exclusively determined by the size of the cavities and not by the angle of incidence of the light. In addition, the modes (K,0) and (0,K) are degenerate inside the cavity. This means that these modes can be excited both with orthogonal and parallel polarization, since the electric field would oscillate along two perpendicular directions. The two modes above can be even excited by unpolarized light, since the latter can be decomposed into two orthogonal linear directions of polarization.

2.3 Strong light-matter coupling in ISB polaritons

An intersubband transition embedded inside a cavity allows to address the light-matter interaction in two different regimes: weak and strong coupling. The latter occurs whenever the coupling constant Ω between the two-level system represented by the ISB transition and the cavity in which it is included is larger than the losses in the system. Peculiar losses to be compared with Ω are the photon decay rate of the cavity γ_c and the transition decay rate γ_{21}, depicted in Figure (2.3). It follows that the system is in *strong coupling regime* whenever $\Omega > \max(\gamma_c, \gamma_{21})$, while it is said to be in *weak coupling regime* when $\Omega < \max(\gamma_c, \gamma_{21})$.

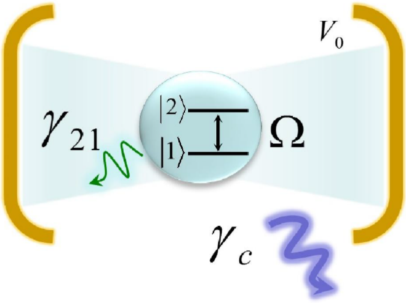

Figure 2.3: A two-level system interacting with a cavity mode. The relevant parameters are the coupling constant Ω, the photon decay rate of the cavity γ_c and the transition decay rate γ_{21}. The strong coupling regime is reached whenever Ω is large compared to γ_c and γ_{21}. From Ref. [7]

The photon emission from a system in the weak coupling regime represents an irreversible process since the emitted photon is unlikely to bounce back towards the two-level system by the walls of the cavity, due to the low coupling constant. However, the emission rate is enhanced by the cavity thanks to the Purcell effect if the latter is at resonance. On the other hand, an emitted photon from a system in strong coupling regime is more likely to be reabsorbed by the two-level system before it is lost from the cavity mode. For this reason, photon emission in the strong coupling regime can be considered as a *reversible* process.

A quantitative description of the interaction between a two-level system and a single mode of an optical cavity is provided by the Jaynes-Cummings model. It takes into account three contributions to the light-matter Hamiltonian. Denoting with $|1\rangle$ and $|2\rangle$ the first and second states of the two-level system respectively, with corresponding energies E_1 and E_2, the matter part of the system is described by the electronic Hamiltonian:

$$H_{\text{mat}} = E_1 |1\rangle\langle 1| + E_2 |2\rangle\langle 2| \ . \tag{2.14}$$

The light part of the system is described instead by the Hamiltonian of an optical resonator:

$$H_{\text{phot}} = \hbar\omega_c \left(a^\dagger a + \frac{1}{2} \right) \ , \tag{2.15}$$

with $\hbar\omega_c$ the quantized energy of a cavity photon hosting a monochromatic field. Finally, the interaction Hamiltonian coupling the two realms can be expressed within the rotating-wave approximation as follows:

$$H_{\text{int}} = -i\hbar\Omega \Big(|2\rangle\langle 1| \, a \ - \ |1\rangle\langle 2| \, a^\dagger \Big) \ , \tag{2.16}$$

The coupling constant of a single ISB transition is defined as [14]:

$$\Omega = \sqrt{\frac{e^2 f_{12}}{4\varepsilon_0 \varepsilon_r m^* V_0}} \ , \tag{2.17}$$

with f_{12} the oscillator strength of the ISB transition between the first two quantum confined states and V_0 the effective volume of the cavity mode. The complete Jaynes-Cummings Hamiltonian can be therefore expressed as the sum of the three contributions:

$$H = H_{\text{mat}} + H_{\text{phot}} + H_{\text{int}} = \begin{pmatrix} \hbar\omega_c & i\hbar\Omega \\ -i\hbar\Omega & \hbar\omega_{21} \end{pmatrix} . \tag{2.18}$$

This merely represents a system composed by two resonators: a cavity with frequency ω_c and a two-level system with frequency ω_{21}, paired together by the coupling constant $\hbar\Omega$. The eigenstates of the Hamiltonian above are called *intersubband-cavity polaritons*, mixed atom-photon states consisting of a linear superposition of electronic excitation and cavity photons. The eigenenergies of the Jaynes-Cummings Hamiltonian in Equation (2.18) show two distinct branches, called *upper* and *lower polaritons*. These can be expressed as a function of the detuning $\Delta E = E_c - E_{21}$ as:

$$E_{\text{UP,LP}} = \frac{1}{2}\left(E_{21} + E_c \pm \sqrt{\Delta E^2 + (2\hbar\Omega)^2}\right) . \tag{2.19}$$

When the detuning ΔE vanishes, the relationship above reduces to $E_{UP,LP} = E_{21} \pm \hbar\Omega$, yielding a minimum energy splitting equal to $2\hbar\Omega$. The upper and lower polariton branches as a function of the detuning are shown in Figure (2.4), highlighting the Rabi splitting. Being a finite quantity, the two polariton branches present a peculiar *anti-crossing*, which is the signature of the strong light-matter coupling regime.

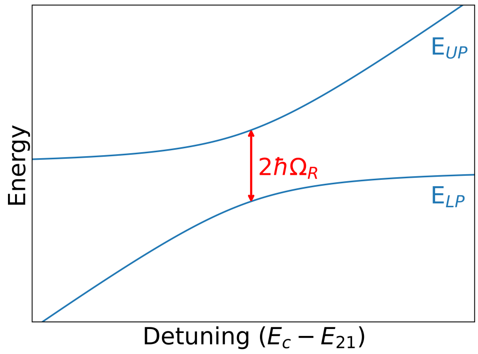

Figure 2.4: Dispersion relation of the two polariton branches as a function of the detuning $\Delta E = E_c - E_{21}$. The minimum distance between the two curves is called Rabi splitting, which is twice the Rabi frequency.

The discussion above concerns a system consisting of a single two level system (namely, a single dipole or electron) embedded inside a cavity. In fact, the device under study is composed by quantum wells in which several intersubband transitions take place. The electromagnetic response of such a structure is dominated by the collective plasmonic excitations of the two-dimensional electron gas, confined within the conduction band of the quantum wells. In first approximation, the frequency splitting – twice the Rabi frequency – can be directly related to the doping through the expression [13]:

$$2\Omega_{\text{Rabi}} = \sqrt{\frac{f_{12}e^2 N_{\text{QW}}(N_1 - N_2)}{\varepsilon\varepsilon_0 m^* L_{\text{cav}}}} , \tag{2.20}$$

where N_{QW} is the number of quantum wells included in the cavity and N_1 and N_2 are the surface electronic population of the fundamental and excited subband, respectively. It follows that the electronic populations N_1 and N_2 can be extracted experimentally from the value of the Rabi splitting $2\Omega_{\text{Rabi}}$. Indeed, under low intensity conditions N_2 can be neglected since all the electrons introduced through doping contribute exclusively to the term N_1, thus representing a reliable gauge of the doping density into the active region.

Chapter 3

Theory of saturation of ISB polaritons

The absorption mediated by intersubband cavity polaritons is well described by coupled mode theory (CMT), which treats the coupling between resonators. This can provide an analytical expression of the intersubband absorption $\mathcal{A}_{\mathrm{ISB}}$ as a function of the characteristic parameters of the oscillators in the system. Afterwards, we will illustrate how to tailor the performance of the device. This is done mainly through two effects: embed the transition inside a cavity to reduce the saturation intensity and achieve a significant change in reflectance at different light intensities.

3.1 Notes on Coupled Mode Theory

Coupled mode theory is a powerful mathematical tool to describe the coupling between oscillators, with or without external excitation governed by wave ports. It characterizes the dynamics of the i-th resonator in the system with four quantities: the amplitude a_i, the eigenfrequency $\omega_i = 2\pi f_i$, the radiative dissipation rate Γ_i and the non-radiative dissipation rate γ_i. The wave ports allow for an incoming single mode s_j^+ to couple with the resonator with a coupling constant κ_{ij}, with the outgoing radiation denoted as s_j^-.

The case under study is best represented within the CMT formalism of two resonators and one port. The cavity mode and the ISB transition are modeled by two resonators subject to the incoming light excitation. The response of the system to the excitation is expressed as [2]:

$$\frac{da_{\mathrm{ISB}}}{dt} = (i\omega_{\mathrm{ISB}} - \gamma_{\mathrm{ISB}})a_{\mathrm{ISB}} + i\Omega_{\mathrm{Rabi}}a_c \ , \tag{3.1}$$

$$\frac{da_c}{dt} = (i\omega_c - \gamma_{nr} - \Gamma_r)a_c + i\Omega_{\mathrm{Rabi}}a_{\mathrm{ISB}} + \sqrt{2\Gamma_r}s^+ \ , \tag{3.2}$$

$$s^- = -s^+ + \sqrt{2\Gamma_r}a_c \ , \tag{3.3}$$

$$n_2 = 2\tau_{12}\gamma_{\mathrm{ISB}}\frac{|a_{\mathrm{ISB}}|^2}{N_{\mathrm{QW}}\hbar\omega} \ , \tag{3.4}$$

with n_2 the surface charge density in the excited subband of the doped QW representing the two-level system. The non-radiative decay rates of the ISB transition and of the cavity are denoted with γ_{ISB} and γ_{nr}, respectively. The radiative decay rate of the cavity is Γ_r, whilst that of the ISB transition can be neglected [3]. The interaction between the ISB transition and the cavity mode is expressed by the coupling rate between them, the vacuum Rabi frequency:

$$\Omega^2_{\mathrm{Rabi}} = f_w \frac{\Delta n \, e^2}{4\varepsilon\varepsilon_0 m^* L_{\mathrm{QW}}} \; , \tag{3.5}$$

where Δn is the electron population difference between the two levels and f_w is the filling fraction of the QW material in the active region.

The absorption of the sole ISB resonator can be evaluated in the harmonic regime ($s^+ = e^{i\omega t}$), returning the maximum value when the two systems are at resonance ($\omega_{\mathrm{ISB}} = \omega_c = \omega_0$), namely [2]:

$$\mathcal{A}^{\mathrm{ISB}} = \frac{4\gamma_{\mathrm{ISB}}\Gamma_r\Omega^2_{\mathrm{Rabi}}}{\{\gamma_{\mathrm{ISB}}(\gamma_{nr}+\Gamma_r) - [(\omega-\omega_0)^2 - \Omega^2_{\mathrm{Rabi}}]\}^2 + (\gamma_{\mathrm{ISB}}+\gamma_{nr}+\Gamma_r)^2(\omega-\omega_0)^2} \; . \tag{3.6}$$

The ISB absorption $\mathcal{A}^{\mathrm{ISB}}$ increases with Ω_{Rabi} as long as the system stays in the weak coupling regime, that is to say for low values of the coupling constant. As soon as the system enters the strong coupling regime for sufficiently high values of Ω_{Rabi}, the maximal absorption saturates to the following value:

$$\mathcal{A}^{\mathrm{ISB}}_{\mathrm{sat}} \approx \frac{4\gamma_{\mathrm{ISB}}\Gamma_r}{(\gamma_{\mathrm{ISB}}+\gamma_{nr}+\Gamma_r)^2} \; . \tag{3.7}$$

3.2 Reduction of the saturation intensity

The saturation intensity is defined as the value of intensity at which the absorption of the system reduces by a factor 2 compared to the low intensity condition. In an ISB system, this condition is reached when the difference in the electron population of the two levels equals half of the sheet electron density n_s coming from doping. This corresponds to $n_1 - n_2 = n_s/2$ or, equivalently, to $n_2 = n_s/4$.

In the weak coupling regime, I_{sat} does not depend on doping and on the number of quantum wells in the active region. For a GaAs/AlGaAs heterostructure with nominal transition between the two levels at 10 μm, a rough estimate of the saturation intensity yields a value around 1 MW/cm^2. It represents a very high value of intensity, thus explaining why SESAMs are currently missing from the toolbox of mid-IR optoelectronic devices. Indeed they would require extremely high power sources to reach absorption saturation, up to values prohibitive for commercially available QCLs. Therefore, it comes naturally the endeavor to drop the value of I_{sat} to make it reachable by current QCL solutions. In this view, the first attempt is to inspect how a cavity affects the saturation intensity, possibly reducing its value. Saturation intensity $I^{\mathrm{WC}}_{\mathrm{sat}}$ actually decreases when the QWs are placed in a cavity [2]:

$$I^{\mathrm{WC}}_{\mathrm{sat}} = f_{12} \frac{\pi L_{\mathrm{AR}}}{\lambda / n_{\mathrm{opt}}} \frac{Q_r}{2(Q^{\mathrm{tot}}_{\mathrm{cav}})^2} I^0_{\mathrm{sat}} \; , \tag{3.8}$$

with f_{12} the ISB oscillator strenght, L_{AR} the total thickness of the active region, and Q_r and $Q^{\mathrm{tot}}_{\mathrm{cav}}$ the radiative and total Q-factor of the cavity, respectively. In Equation (3.8), the cavity-free saturation intensity is denoted as I^0_{sat}, hence allowing us to address the parameters which mainly affects the saturation intensity when the QWs are placed in the cavity. Considering fixed the ISB oscillator strength, two degrees of freedom are left to reduce I_{sat}. The first comes by reducing L_{AR}, thus compressing the cavity electric field in ultrasubwavelength volumes. The second relies on the optimization of the branching ratio of the two cavity quality factors Q_r and $Q^{\mathrm{tot}}_{\mathrm{cav}}$. This would require a minimization of the material losses to achieve a large Q_{nr}. The present circumstance is summarized in Figure (3.1), showing the saturation intensity as a function of doping either with or without a cavity. Once in the weak coupling regime, I_{sat} is reduced by two orders of magnitude, down to values affordable with the typical output power levels of QCLs.

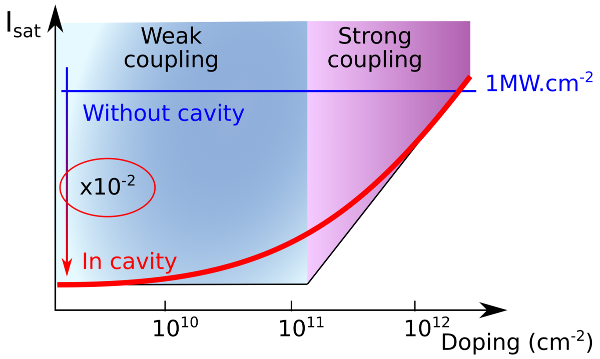

Figure 3.1: Saturation intensity as a function of doping in both weak and strong coupling regime, representing both the situation without the cavity I^0_{sat} and with the cavity $I^{\text{WC}}_{\text{sat}}$. The saturation intensity in weak coupling regime is reduced by two orders of magnitude by placing the transition inside a cavity [2].

3.3 Collapse of the strong light-matter coupling and induced reflectivity change

Besides the reduction of the saturation intensity obtained by placing the ISB transition inside a cavity, the second effect to enable the desired operation of the device is to play with the optical response of the system, represented in Figure (3.2). The reflectance spectrum of the device at low illumination intensity – red curve in Figure (3.2a) – presents two dips (corresponding to the two *polariton branches*) separated in frequency by $2\Omega_{\text{Rabi}}$. The reflectance spectrum visibly changes upon high intensity condition – blue curve in Figure (3.2a) – showing the collapse of the light-matter interaction. In this circumstance, only one reflectance dip is present, corresponding to the response of the bare cavity. The peculiar modification of the spectral response of the system under different illumination conditions yields a strong spectral feature in terms of change in reflectance. This phenomenon is particularly evident at the two polariton frequencies, highlighted by the two blue shaded regions in Figure (3.2a). The spectral response at these two wavelengths moves from low reflectance at low intensity to high reflectance at high intensity, hence matching the conditions for a SESAM, as detailed in section (1.2).

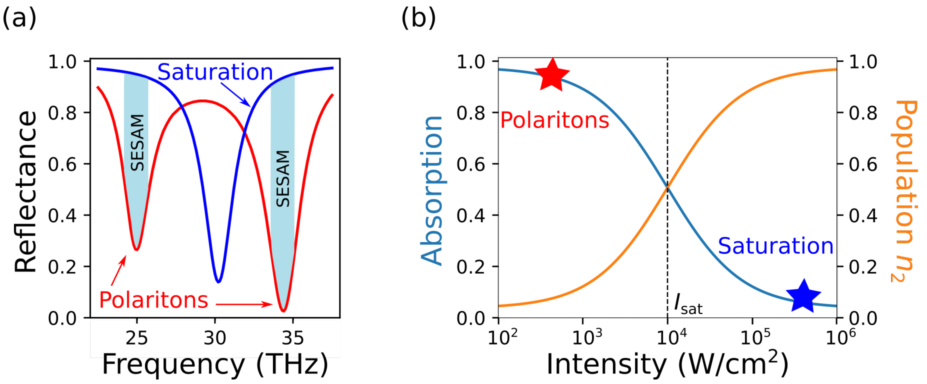

Figure 3.2: (a) Optical response under low (red curve) and high intensity (blue curve). At the frequencies highlighted by blue shaded regions a strong spectral feature in terms of change in reflectance is produced, thus representing a SESAM. (b) Behavior of the absorption and the electron population n_2 as a function of the intensity, typical of a saturable absorber. The red and blue stars refer to the optical response at low and high intensity, respectively.

Chapter 4

Experimental characterization of ISB polaritons and saturation

This section is mainly devoted to illustrate the experimental results obtained during the internship. I did not fabricate the samples myself, however a brief illustration of the main fabrication steps is provided in the following. The devices were characterized using two different optical setups, under low and high illumination intensity. The analysis reports a tangible spectral feature, witnessing a non linear response of the system and paving the road for the concept of SESAMs in the mid-IR.

4.1 Description of the samples

The structures under study are arrays of semiconductor multi-quantum-wells stacked between two metal layers, as shown in Figure (4.1a). In Figure (4.1b) it is reported an electron microscope picture of the sample, containing several square patches. The active region is composed by 7 GaAs/AlGaAs quantum wells, while the cavity walls are made of gold. The size of each squared QW is expressed with s and the spacing between them with p, both parameters in the order of 1 μm. The period is therefore given by $s + p$.

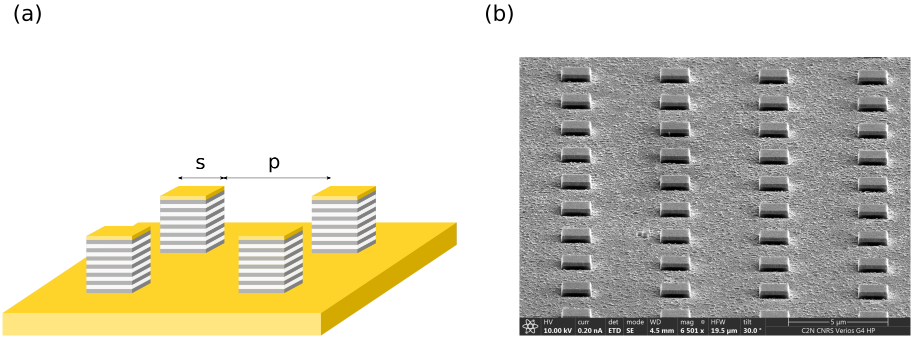

Figure 4.1: (a) Array of 7 GaAs/AlGaAs multi-quantum-wells stacked between two layers of gold, with varying geometrical parameters s and p. (b) SEM picture of the same structures.

The main fabrication steps are briefly detailed in the following. The active region containing the QWs is produced through molecular beam epitaxy on a semiconductor substrate. An adhesion layer of Ti and a metallic layer of Au is deposited on the active region, as well as on top of a host substrate. The two are bonded together by their metallic surfaces via thermo-compressive wafer bonding. The substrate of the active region is then removed through manual polishing and chemical etching, up to an etch-stop layer which had been grown before the active region during epitaxy. On the uncovered active region, the squared patches are later realized. A layer of resist is deposited on the upper side of the active region, which is then patterned through electron-beam lithography. After the development, it follows a metal deposition of gold on the whole area. A lift-off step is employed to selectively remove gold and return the desired array of square patches including the active regions. Finally, a dry etch step using the square metal patches as a mask, leaving the semiconductor active region only below the microcavities.

The samples contain several arrays of microcavities with different geometrical parameters, in order to address a specific optical response in reflectance. Furthermore, the quantum wells in the active region can be properly doped, implying a change in the Rabi frequency, as highlighted in Equation (3.5). In this work I performed the measurements on multiple samples presenting different nominal doping per QW: HM4445 (no doping), HM4447 (1.1×10^{12} cm^{-1}) and HM4448 (1.5×10^{12} cm^{-1}).

4.2 Measurements at low input intensity

The samples have been initially characterized under low intensity condition to evidence the two polariton dips in the reflectance spectra. This has been done by Fourier transform infrared (FTIR) spectroscopy, a technique to collect the reflectance spectra of a sample. Its major advantage with respect to dispersive spectroscopy relies on the possibility to acquire the spectrum on a broad range of wavelengths at a time. A polychromatic light source shines into a Michelson interferometer – an optical setup including a beam-splitter and two mirrors, one of which movable. As the movable mirror runs along its rail, light interference between the two light beams periodically blocks and transmits the individual wavelengths composing the polychromatic beam. In this way the spectrum of the light coming out from the interferometer is modulated according to the position of the movable mirror. It follows that the raw data of this technique are composed by the reflectance spectra related to the mirror position (also called interferograms). Afterwards, a computer performs a Fourier transform to relate the resulting spectrum to the wavelength of the light. The FTIR used for this work is equipped with an MCT detector, a KBr beam-splitter and a Globar IR source. The measurements were acquired 50 times for each spectrum with a resolution of 4 cm^{-1}.

On a practical side, the reflectivity spectrum of each sample was normalized to the reflectivity spectrum of a reference gold pad. This produces a spectrum of the normalized reflectance of the sample as a function of the light wavenumber. For the two doped samples HM4447 and HM4448, the spectra show two reflectance dips corresponding to the upper and lower polaritons, as expressed in Equation (2.19). On the contrary, the spectra of the undoped sample HM4445 presents only one reflectance dip, corresponding to the absorption of the cavity mode, since the ISB transition is disabled in undoped quantum wells. In addition, the reflectance spectra change with the geometrical parameters s and p of the sample. Figure (4.2) shows the reflectance spectra of samples HM4445 and HM4447 for the same value of (fixed) spacing $p = 2$ μm and varying values of size s ranging from 1.20 to 1.35 μm.

The spectra reported in Figure (4.2) are characterized by one or two reflectance dips, located at a given wavenumber. All these features are fitted with a Lorentzian model to extract the position of the minima and the width of the dip. For sample HM4445 the fit is done with a single Lorentzian dip, with a baseline at unity:

$$R = 1 - \frac{A}{\pi}\left[\frac{\sigma}{(x-\mu)^2+\sigma^2}\right] , \tag{4.1}$$

while for sample HM4447 the model is a double Lorentzian dip to account for the contribution of the two polariton branches:

$$R = 1 - \frac{A_1}{\pi}\left[\frac{\sigma_1}{(x-\mu_1)^2+\sigma_1^2}\right] - \frac{A_2}{\pi}\left[\frac{\sigma_2}{(x-\mu_2)^2+\sigma_2^2}\right] . \tag{4.2}$$

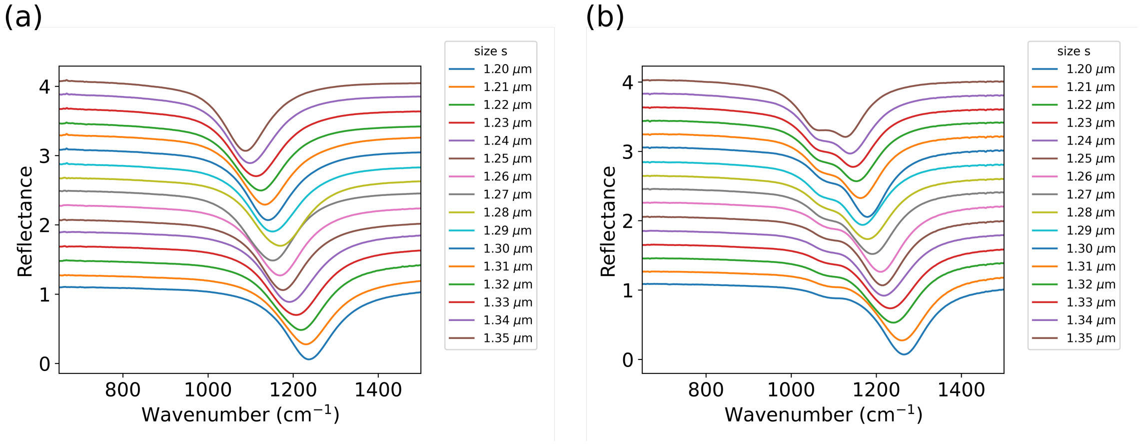

Figure 4.2: Reflectance spectra for HM4445 (a) and HM4447 (b) for $p = 2$ μm. The spectra have been offset for clarity.

Figure (4.3) presents the result of the fit for both samples, with single and double Lorentzian dip model. The position of the minima are plotted as a function of the cavity size s in the right panels of Figures (4.3a) and (4.3b). The reflectance minima of sample HM4445 correspond to the cavity wavenumber, while the reflectance minima of sample HM4447 correspond to the two polaritons wavenumbers.

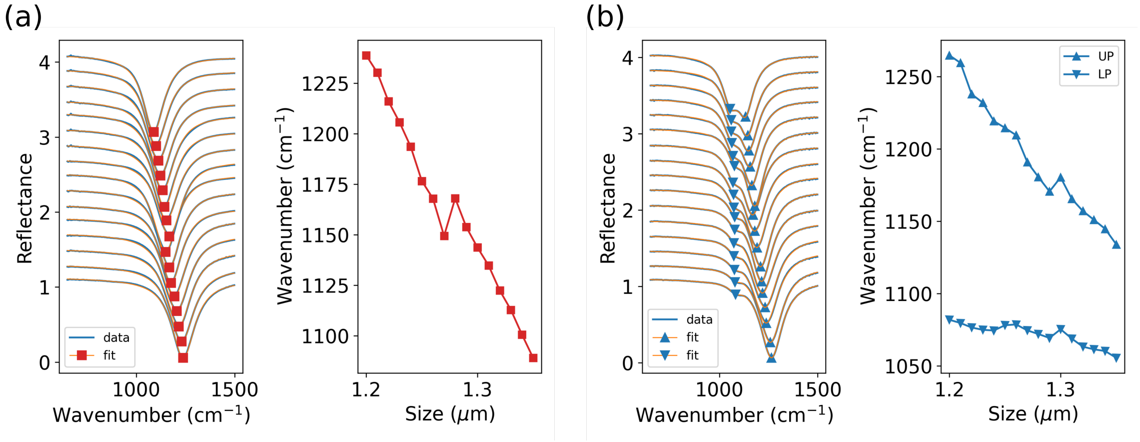

Figure 4.3: Single and double Lorentzian dip fit for $p = 2$ μm to extract the position of the minima of reflectance. The right panels of both figures report the reflectance minima as a function of s, corresponding to the cavity wavenumber for sample HM4445 (a) and the polaritons wavenumber for sample HM4447 (b).

From the dispersion relation of the undoped cavity HM4445 it is possible to extract the effective modal index n_M of the QWs in the active region, through the relationship [10]:

$$\nu_K = \frac{K}{2n_M}\frac{1}{s}\ , \tag{4.3}$$

with ν_K the resonant frequencies (expressed in cm$^{-}1$) of the reflectance dips in the undoped cavity, K an integer denoting the mode and s the size of the square patch. The cavity wavenumbers result from the single Lorentzian fit in Figure (4.3a). At sub-wavelength cavity thickness – as in the case of the present work – the cavity mode can only host the lowest order guided TM$_0$ mode which does not present a cut-off frequency. For this reason, in the following discussion we will assume $K = 1$. The plot of the cavity wavenumbers ω_c as a function of the inverse of the patch size is reported in Figure (4.4), together with the linear fit resulting from Equation (4.3).

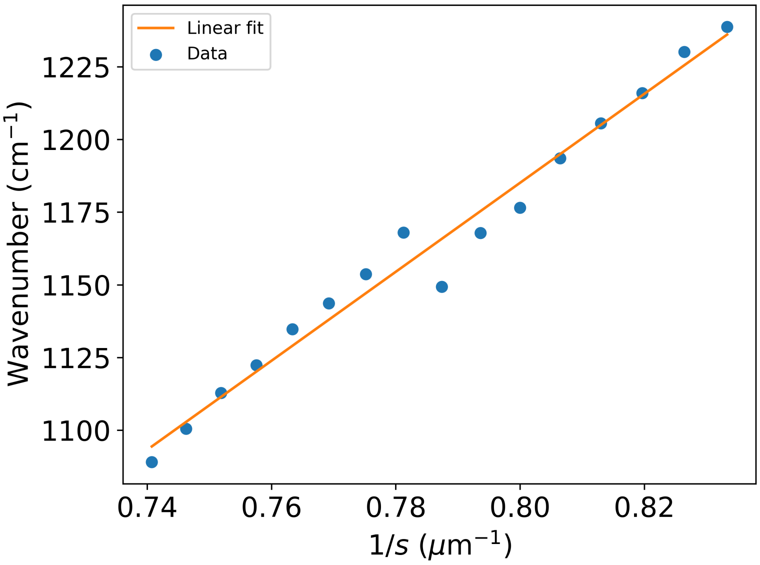

Figure 4.4: Cavity wavenumbers as a function of the inverse of the patch size for sample HM4445 and $p = 2\ \mu$m. The linear fit is made on Equation (4.3), returning $n_M = 3.27$.

Table (4.1) reports the values of n_M for different spacing p extracted through the linear fit of Equation (4.3) on the refletance minima of sample HM4445. The measure of n_M for more spaced patches (higher p) matches with the bulk refractive index of GaAs in the infrared range, which is equal to 3.3, whereas for closer resonators the measured n_M is up to 14% higher than the value in the bulk. We can ascribe this imbalance to the impedance mismatch at the edges of the resonators that confines the electromagnetic field within the structures [12]. This effect is more pronounced in less separated resonators, as the electric field confined in each of them could leak out and enter the neighboring structures, inducing *cross-talking* between them.

Spacing p	Effective modal index n_M
1 μm	3.78
1.5 μm	3.53
2 μm	3.27

Table 4.1: Experimental results for the effective modal index n_M for the different values of spacing p.

The cavity and the two polariton branches are plotted together in the same graph in Figure (4.5a). It clearly reports a bump in the trend of the reflectance minima as a function of the size, for both samples HM4445 and HM4447. This feature is due to an artifact during the electron beam lithography, which causes the nominal sizes of the patches at the edges of the sample to differ from their actual values. Since the nominal value of s does not offer a neat view on the dispersion relation, the polaritons wavenumbers are plotted as a function of the sorted cavity wavenumber in Figure (4.5b). Upward and downward triangles denote upper and lower polaritons, respectively. These data are fitted with the following secular equation [11]:

$$(\omega^2 - \omega_c^2) \times (\omega^2 - \omega_{21}^2) = \Omega_{\text{Rabi}}^2\ \omega_c^2\ , \tag{4.4}$$

where ω_{21} is the ISB transition frequency and Ω_{Rabi} the Rabi frequency. In turn, the latter serves to define the Rabi splitting as $2\Omega_{\text{Rabi}} = \sqrt{\Gamma_{\text{opt}}\ f_w}\ \omega_p$, where Γ_{opt} is the *electromagnetic overlap* which expresses the overlap between the electric field distribution in the cavity mode and the semiconductor QWs embedded in the active region

$$\Gamma_{\text{opt}} = \frac{\iiint_{\text{active region}} |E_z|^2 \, d\vec{r}}{\iiint_{\text{cavity mode volume}} |E|^2 \, d\vec{r}} \, , \tag{4.5}$$

f_w is the *quantum well overlap factor* accounting for the fraction of QW layers within the whole active region stack

$$f_w = \frac{L_{\text{QW}}}{L_c} \, , \tag{4.6}$$

ω_p is the electronic plasma frequency in the quantum well

$$\omega_p = \sqrt{\frac{n_e \, e^2}{\varepsilon\varepsilon_0 \, m^* L_{\text{QW}}}} \tag{4.7}$$

and ω_c is the cavity frequency. The two polariton branches in Figure (4.5b) are relatively far at high values of cavity wavenumber, getting closer with lower values of ω_c. They reach a minimum distance between each other and then slightly diverge again for very low values of ω_c. This behavior is called *anti-crossing*, representing a clear signature of the strong light-matter coupling regime taking place in the ISB transition.

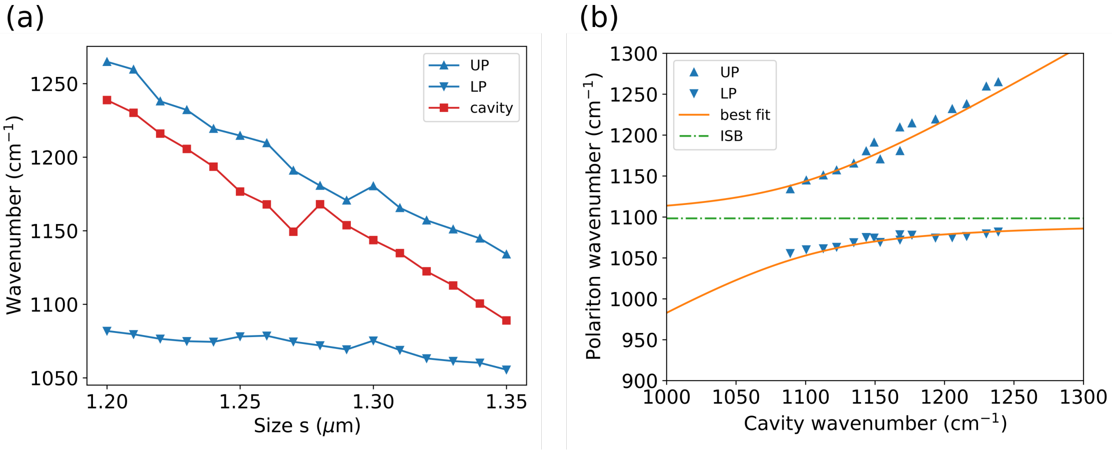

Figure 4.5: (a) Plot of the cavity and the polaritons wavenumbers as a function of the size s. (b) Polariton wavenumber as a function of the cavity wavenumber. The data are fitted with the analytical expression of the secular equation (4.4). Fixed spacing $p = 2$ μm.

The fit of the experimental data with the roots of Equation (4.4) allows to extract significant parameters, such as the Rabi frequency Ω_{Rabi} and the ISB transition frequency ω_{21}. These are reported in Table (4.2), which contains the experimental parameters of sample HM4447 for all the three values of spacing p.

Spacing p	Rabi frequency Ω_{Rabi}	Transition frequency ω_{21}	Ratio $\Omega_{\text{Rabi}}/\omega_{21}$
1 μm	46 cm^{-1}	1115 cm^{-1}	4 %
1.5 μm	48 cm^{-1}	1103 cm^{-1}	4 %
2 μm	45 cm^{-1}	1098 cm^{-1}	4 %

Table 4.2: Experimental values of Rabi frequency and transition frequency for sample HM4447, for all the three values of the spacing p. Other parameters are: $\Gamma_{\text{opt}} = 1$ and $f_w = 0.135$.

Furthermore, from the Rabi splitting – that is the minimum separation between the two polariton branches – it is possible to retrieve the actual value of the doping present in the active region QWs. This is made possible by the explicit relationship between the Rabi frequency and the doping expressed in Equation (3.5). The latter equation includes the difference in electron population Δn between the first and the second level of the QW. However, at the low intensity values addressed by the FTIR measurements, we assume that no ISB transition is allowed within the two quantum confined levels. In this condition we can assume $n_2 \approx 0$, hence $\Delta n \approx n_1$. Therefore, a direct link establishes between the doping n_s and the measured Rabi frequency Ω_{Rabi}:

$$\Omega_{\mathrm{Rabi}} = \sqrt{\frac{n_s N_{\mathrm{QW}} e^2 f_{12}}{4\varepsilon_0 \varepsilon_r m^* L_c}} \,, \tag{4.8}$$

with n_s the sheet doping in the QWs, N_{QW} the number of QWs, ε_r the relative dielectric constant of the well material and L_c the length of the cavity. The equation above can be inverted to retrieve the expression of the doping:

$$n_s = \frac{4\varepsilon_0 \varepsilon_r m^* L_c}{N_{\mathrm{QW}} e^2 f_{12}} \Omega_R^2 \,. \tag{4.9}$$

Considering the experimental value of Rabi frequency equal to $2\pi \times 1.39$ THz, $N_{\mathrm{QW}} = 7$, $f_{12} = 0.961$, $L_c = 192$ nm, $\varepsilon_r = 12.88$ and $m^* = 0.063\ m_e$ for GaAs, the experimental doping value turns out to be around 2.8×10^{11} cm^{-2}. This appears to be much lower than the nominal value doping of 1.1×10^{12} cm^{-2}.

4.3 Measurements at high input intensity

The samples have been characterized under high intensity as well, to investigate the collapse of the light-matter interaction and induce absorption saturation. This is done with a more complex optical setup – sketched in Figure (4.6) – using a QCL (MIRCat from Daylight Solutions) as laser source in the mid-IR. The sample is placed in front of a microscope objective in a confocal configuration. Light reflected from the sample is collected by a semi-reflecting mirror. With a system of mirrors, the light beam can be sent either to an IR camera MIR-Cam or to an MCT detector D. The camera is needed to observe the right positioning of the sample in order to address the desired values of s and p. The detector is instead connected to a lock-in amplifier LI, which returns a value of power of the detected light. All the measurements were performed at room temperature.

The setup here described allows to investigate the response of the system under different conditions. The laser source can scan a range between 1016 and 1325 cm^{-1} using two different laser chips. Additionally, two different methods can be used to control the intensity of the incoming laser light. An optical block composed by a half-wave plate and a polarizer in series is placed in the excitation path. The half-wave plate can be rotated with a mechanical actuator while the position of the linear polarizer is fixed. Upon the rotation of the half-wave plate, the intensity of the light coming out from the polarizer can be tuned, being maximum when the two directions are parallel and minimum when they are perpendicular. This results in a sinusoidal behavior of the magnitude coming from the optical block, as measured in Figure (4.7). The calibration of the optical block allowed to determine the angles of the half-wave plate yielding the minimum and the maximum of intensity, corresponding to 34 and 80 degrees respectively. The driving current of the laser can also be tuned between 570 mA – the lasing threshold – and 880 or 1000 mA, depending on the chip in use. This represents a second way to address different illumination conditions on the sample. By combining the current on the QCL and the angle θ of the half-wave plate, it is possible to scan the intensity of the light impinging on the sample over a range of two orders of magnitude. Finally, another polarizer is placed in the detection branch to control the intensity of the light reaching the detectors and ensure that they operate in a linear detection regime.

Although the measurement at high intensity returns again a reflectance spectrum of the sample, this technique differs from the FTIR spectroscopy discussed in the previous section. In the present case the source of light is a QCL with tunable current, emitting

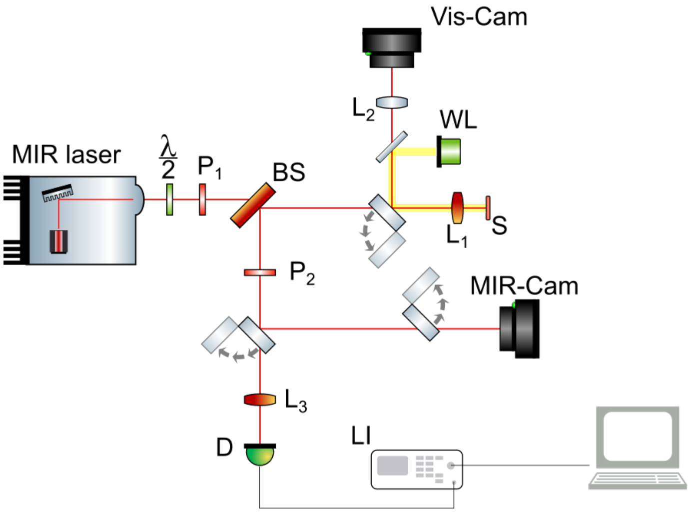

Figure 4.6: Sketch of the experimental setup to measure the reflectance spectra of SESAMs. The source is a commercial tunable mid-infrared QCL (Daylight Solutions 1010-1350 cm^{-1} emitted wavelengths at 400 mW maximum average power). The intensity of the light coming to the sample S can be adjusted by regulating the current on the laser or by rotating the axis of the half-wave plate $\lambda/2$ with respect to the fixed polarizer P_1. The back reflected beam is collected through the beam-splitter BS, and sent to the detector D (MCT Teledyne detector, LN-cooled). The electrical signal from the detector is sent to a lock-in amplifier LI (Stanford Research System). WL white light, Vis-Cam visible camera, MIR-Cam MIR camera.

monochromatic radiation within 1016 and 1325 cm^{-1}. Therefore, to acquire an entire spectrum the wavelength of the laser must be sequentially scanned over time, whereas in the FTIR spectroscopy the measurements were taken all at once. The optical setup is controlled through a Python interface, allowing to automatize the data acquisition.

The measurements at FTIR allow to choose the sample to be later analyzed under high intensity condition. Figure (4.5) clearly shows that, for $p = 2$ μm, the lowest Rabi splitting between the two polaritons is shown at $s = 1.35$ μm, hence indicating the resonance condition between the cavity and ISB transition. The same applies also for the other available values of p, thus the next measurements will focus on samples with $s = 1.35$ μm. Then it is left to choose the value of p presenting the highest reflectance contrast. Figure (4.8) shows the FTIR reflectivity spectra at fixed $s = 1.35$ μm and different p (the curves have been vertically aligned at unitary reflectance). Comparing the three curves, it turns out that the highest contrast is achieved by $p = 1$ μm (blue curve), which is therefore chosen for the next measurements. Hence, the sample presenting the most favorable condition to achieve saturation under high intensity condition is $s = 1.35$ μm and $p = 1$ μm.

I then measured the reflectance spectra of the sample described above to observe how the optical response of the system changes under different illumination intensity. This was done at two different values of light intensity, scanning the whole wavelength spectrum on the two chips of the laser. In particular, it was addressed either a linear regime at low intensity to show the two polariton branches in the reflectance spectrum, or a non-linear regime at high intensity to cause the collapse of the two polaritons and hence to induce the absorption saturation.

Figure (4.9) reports the result of this first set of measurements on sample HM4447. At low intensity (dashed line), the whole wavelength spectrum on the two chips of the laser could be exploited, whereas at high intensity (solid line) only one chip could be used, limiting the wavelength spectrum to a narrower range. The former was obtained experimentally with the half-wave plate at 34° and laser current at 570 mA; the latter instead is obtained by removing the optical block containing the wave-plate and the fixed

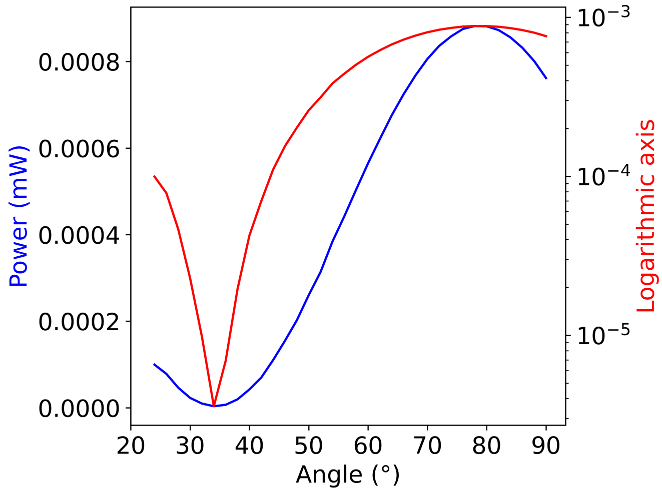

Figure 4.7: Calibration of the optical block: magnitude of the signal on the detector as a function of the angle of the half-wave plate. The intensity of the light varies in a sinusoidal fashion with the angle, returning a minimum at 34° and a maximum at 80°. Logarithmic scale on the right axis helps to identify the position of the minimum corresponding to 34°.

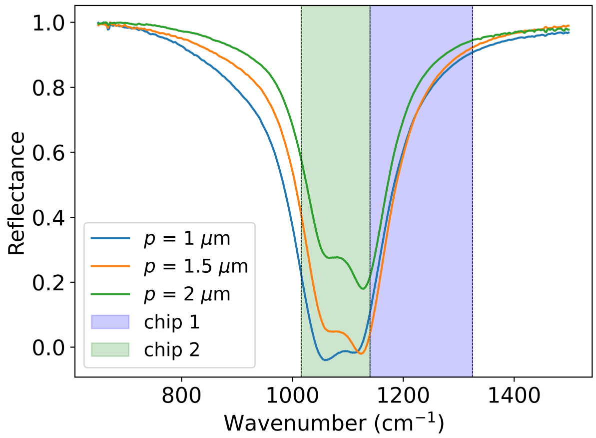

Figure 4.8: Reflectivity spectra of sample HM4447 at low intensity FTIR for $s = 1.35\ \mu$m and different spacings p. The highest contrast in terms of reflectance is offered by $p = 1\ \mu$m.

polarizer and by setting the laser current at 1000 mA. These represent the extremes of low and high intensity condition reachable by the current setup.

The results at this stage already show a strong spectral feature in terms of change in reflectance moving from low to high intensity condition. Indeed, the two curves shown in Figure (4.9) highlight the collapse of the strong light-matter coupling and the absorption saturation in the device. However, the change in reflectance is more evident at some wavelengths than others. At 1080 cm^{-1}, corresponding to the frequency of the cavity, the reflectance decreases with the impinging intensity. On the contrary, at 1052 and 1112 cm^{-1} – which correspond to the two polariton frequencies – the reflectance increases with the intensity. This second case well describes the behavior of a SESAM, namely a mirror showing low reflectance at low intensity and high reflectance at high intensity.

To further analyze the optical response of the system, the reflectance has been measured at fixed wavelengths and varying light intensity. In order to follow the behavior of the reflectance as a function of the intensity, three different experimental regimes were tested. The first ones are at driving laser current of respectively 570 mA and 1000 mA, varying the angle θ of the half-wave plate from 34° to 80°. The third regime is obtained

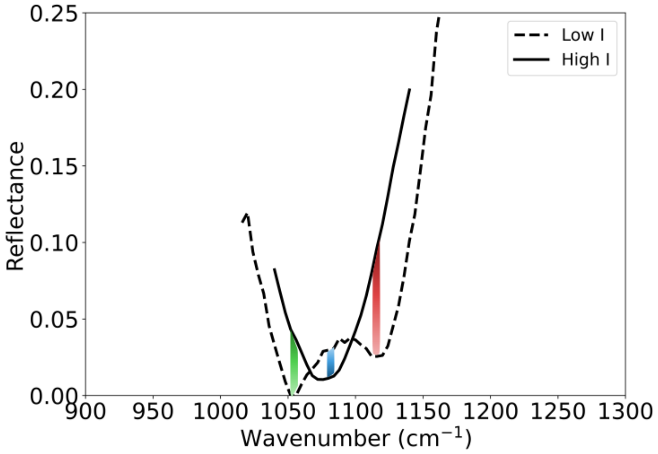

Figure 4.9: Reflectance spectra at low and high intensity of sample HM4447, with $s = 1.35\ \mu$m and $p = 1\ \mu$m. The change in the optical response can be appreciated as a change in the reflectance. At low intensity the system shows two reflectance dips corresponding to the polaritons, while at high intensity the two dips collapse to the response of the cavity.

without the block containing the half-wave plate and the fixed polarizer in order to address the highest possible intensity, by varying the driving current of the QCL from 570 mA to 1000 mA. Afterwards, these three sets of measurements were merged to monitor the reflectance of the device with impinging intensity ranging between tens of W/cm^2 and tens of kW/cm^2. The intensity of the beam impinging on the sample was calibrated using a power meter. The pulse rate is set at 10 kHz and the pulse width at 500 ns, yielding a duty cycle of 0.5 %. Therefore, the peak power is obtained by dividing the power given by the lock-in amplifier by 5 × 10^{-3}. Finally, to convert into an intensity value, the peak power was divided by the beam surface. The beam radius at the focal point w_f can be retrieved by the following expression:

$$w_f = \frac{\lambda f}{\pi w_0}\ , \tag{4.10}$$

with $f = 12$ mm the focal length in the IR range, $\lambda \approx 10\ \mu$m the wavelength in use and $w_0 = 2$ mm the radius of the beam impinging on the lens L$_1$. This yields a beam radius at the focal point equal to 20 μm.

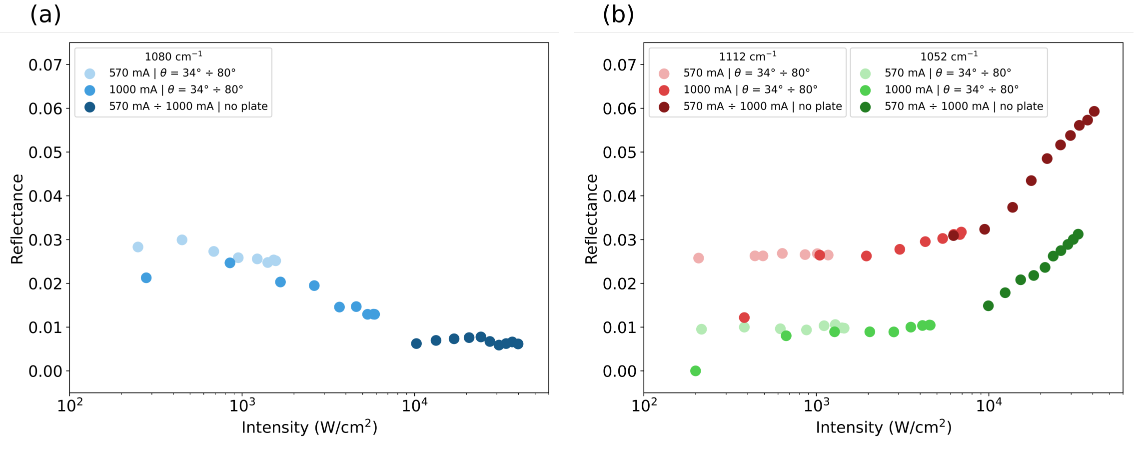

Figure 4.10: Reflectance spectra of sample HM447, with $s = 1.35\ \mu$m and $p = 1\ \mu$m, at wavenumber corresponding to cavity (a) and polaritons (b).

Figure (4.10) reports the plot of the reflectance as a function of the light intensity impinging on the sample, resulting from matching together the three sets of measurements to scan the intensity over more than two orders of magnitude. These results must be directly related to those shown in Figure (4.9), in order to better understand the behavior of the reflectance. The vertical colored bars denote the wavelengths that were analyzed with the QCL setup scanning the light intensity. In both Figures (4.9) and (4.10) faint shade represents low light intensity, whereas strong one represents high light intensity. At 1080 cm^{-1}, the wavenumber corresponding to the cavity mode, the reflectance decreases from 0.03 to 0.005, as reported in Figure (4.10a), yielding a variation of around 80 % in the reflectance. On the other hand, at 1052 and 1112 cm^{-1}, the wavenumbers corresponding to the lower and upper polaritons respectively, the reflectance increases with the intensity. For both polaritons wavenumbers, the reflectance changes by about 50 %. The one shown in Figure (4.10b) represents a neat example of the non-linear optical response of a SESAM: low reflectance at low intensity and high reflectance at high intensity.

Chapter 5

Future perspectives

Several improvements can be envisioned to further push the performance of the device, although the results shown in the previous section are already promising towards the realization of saturable absorber mirrors in the mid-IR. A first advance in the direction of enhanced ΔR is the improvement of the Q-factor of the microcavity, yielding a better contrast in the reflectance spectra. Furthermore, the dynamics of the system can be investigated to better understand the time scale of the ISB processes.

5.1 Improvement of the cavity Q-factor

The *quality factor*, or Q-factor, of a resonator describes how fast the oscillation dampens due to internal losses. It is defined as the ratio between the central frequency f_0 of the resonator and its full width at half maximum Δf:

$$Q = \frac{f_0}{\Delta f} \ . \tag{5.1}$$

Having a large Q-factor is desirable to have higher contrast, that is the difference between the reflectance in high and low intensity regime. This is clearly visible in Figure (5.1), which compares the optical response of two systems having different Q-factors but the same value of polariton splitting $2\Omega_{\text{Rabi}}$. The difference in reflectance ΔR in correspondence of the two polariton wavenumbers significantly changes by properly improving the Q- factor.

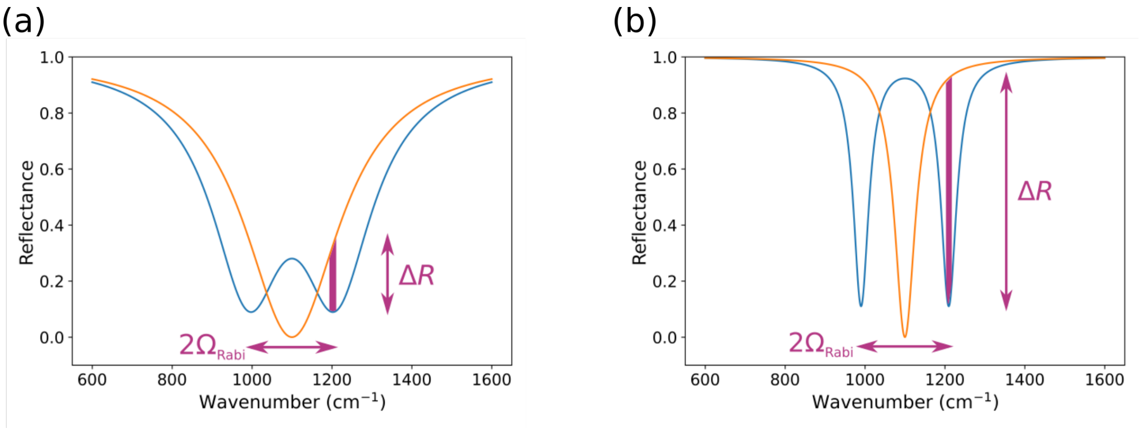

Figure 5.1: Comparison between the optical response of microcavities with Q-factor equal to 15 (a) and 70 (b), and same polariton splitting $2\Omega_{\text{Rabi}}$.

There are two oscillators involved in the process which can be subject to the improvement of the Q-factor: the cavity mode and the ISB transition. To increase the latter, some improvements can be proposed. On one hand, the titanium adhesion layer could be removed from the gold layers. On the other hand, the gold layers composing the mirror could be substituted by photonic crystals. These are composed by dielectrics, presenting negligible losses compared to metal and hence offering higher Q-factor.

5.2 Ultra-fast characterization of the SESAM

A crucial step to investigate the dynamics of the system is to characterize the electron population in the excited level of the quantum wells inside the active region. This must be done on an ultra-fast time scale due to the rapid decay of the electron population in the ISB transition, which is of the order of few picoseconds [5]. Such an analysis is made possible using Optical Parametric Oscillators (OPOs), of the kind discussed in Section (1.1). An OPO represents a powerful asset which can be employed in the context of pump-probe experiments. In this kind of experiments, a sample is shined with two beams: a pump and a probe, with usually lower intensity than the pump. The former starts the ISB transition inside the QW, promoting the electrons to the excited level. Simultaneously, the probe beam monitors the electron population inside the well: since the intensity of this radiation is very weak, it can promote only a negligible portion of electrons, thus leaving the electron density almost unaffected. By properly setting a time delay between the two beams, it is possible to monitor the time dependence of the phenomenon inside the cavity.

5.3 Demonstration of mode-locking in the mid-IR

Thanks to the development of SESAMs in the mid-IR, it would be possible to achieve spontaneous mode-locking in mid-IR lasers by delivering an extremely compact technology to produce pulsed light. The kernel of the idea is the strong coupling regime inside the SESAM, where the intra-cavity intersubband transition can be tuned within the mid-IR from 5 to 14 μm in wavelength. This is made possible by judiciously selecting the composition of the active region, from GaAs/AlGaAs to InGaAs/AlInAs. With this innovative approach it will be possible to demonstrate passive mode-locking in interband cascade lasers, mid-IR VCSELs and fiber lasers. The ultimate goal is to enable ultrafast, energy efficient and compact laser sources in the mid-IR.

Bibliography

[1] Jonas Heidrich et al. “Full optical SESAM characterization methods in the 1.9 to 3-μm wavelength regime”. In: *Optics Express* 29.5 (2021), pp. 6647–6656.

[2] Mathieu Jeannin, Jean-Michel Manceau, and Raffaele Colombelli. “Unified description of saturation and bistability of intersubband transitions in the weak and strong light-matter coupling regimes”. In: *Physical review letters* 127.18 (2021), p. 187401.

[3] Mathieu Jeannin et al. “Absorption engineering in an ultrasubwavelength quantum system”. In: *Nano letters* 20.6 (2020), pp. 4430–4436.

[4] Ursula Keller et al. “Semiconductor saturable absorber mirrors (SESAM’s) for femtosecond to nanosecond pulse generation in solid-state lasers”. In: *IEEE Journal of selected topics in QUANTUM ELECTRONICS* 2.3 (1996), pp. 435–453.

[5] M Knorr et al. “Intersubband polariton-polariton scattering in a dispersive microcavity”. In: *arXiv preprint arXiv:2201.05056* (2022).

[6] Dmitri E Nikonov et al. “Collective intersubband excitations in quantum wells: Coulomb interaction versus subband dispersion”. In: *Physical review letters* 79.23 (1997), p. 4633.

[7] Bruno Paulillo. “Circuit-tunable subwavelength terahertz devices”. Theses. Université Paris Saclay (COmUE), June 2016. URL: https://tel.archives-ouvertes.fr/tel-01544686.

[8] Zhipeng Qin et al. “Semiconductor saturable absorber mirror in the 3–5 μm mid-infrared region”. In: *Optics Letters* 47.4 (2022), pp. 890–893.

[9] Evgeni Sorokin et al. “Femtosecond sesam-modelocked cr: Zns laser”. In: *Optics express* 20.27 (2012), pp. 28947–28952.

[10] Y Todorov et al. “Strong light-matter coupling in subwavelength metal-dielectric microcavities at terahertz frequencies”. In: *Physical review letters* 102.18 (2009), p. 186402.

[11] Yanko Todorov and Carlo Sirtori. “Intersubband polaritons in the electrical dipole gauge”. In: *Physical Review B* 85.4 (2012), p. 045304.

[12] Yanko Todorov et al. “Optical properties of metal-dielectric-metal microcavities in the THz frequency range”. In: *Optics express* 18.13 (2010), pp. 13886–13907.

[13] Yanko Todorov et al. “Polaritonic spectroscopy of intersubband transitions”. In: *Physical Review B* 86.12 (2012), p. 125314.

[14] Pierre-Baptiste Vigneron. “Mid-Infrared Detectors and THz Devices Operating in the Strong Light-Matter Coupling Regime”. Theses. Université Paris Saclay (COmUE), Apr. 2019. URL: https://tel.archives-ouvertes.fr/tel-02298382.

[15] Eicke R Weber et al. *Intersubband transitions in quantum wells: physics and device applications*. Academic press, 1999.

[16] Jean Wei et al. “A semiconductor saturable absorber for mid-infrared wavelengths”. In: *CLEO: Science and Innovations*. Optical Society of America. 2013, CW3H–3.